Applied Energy 360 (2024) 122803

Contents lists available at ScienceDirect

Applied Energy

journal homepage: www.elsevier.com/locate/apenergy

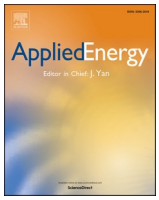

Rapid prediction of particle-scale state-of-lithiation in Li-ion battery microstructures using convolutional neural networks

Sam Ly, Mohammad Amin Sadeghi, Niloofar Misaghian, Hamed Fathiannasab, Jeff Gostick *

Department of Chemical Engineering, University of Waterloo, Ontario, Canada

HIGHLIGHTS

- Machine learning was used to accelerate microstructural simulations of LiB discharge.
- The model predicted the microstructural distribution of lithium throughout the electrode.
- The state-of-lithiation gradients within individual particles was captured.
- Predictions were verified at different C-rate and depth of discharge.

ARTICLE INFO

Keywords:
*li*thium-ion batteries
State-of-lithiation
Microstructure
Convolutional neural networks
Machine learning

ABSTRACT

A machine learning (ML) model was developed to study the discharge behaviour of a $Li_xNi_{0.33}Mn_{0.33}Co_{0.33}O_2$ half-cell with particle-scale resolution. The ML model could predict the state-of-lithiation of the particles as a function of time and C-rate. Although direct numerical simulation has been well established in this area as the prevalent method of modeling batteries, computational expense increases going from 1D-homogenized model to particle-resolved 3D models. The present ML model was trained on a total of sixty different electrodes with various lengths for a total of 4 different C-rates: 0.25, 1, 2, and 3C. The ML model used convolutional layers, resulting in an image-to-image regression network. To evaluate model performance, the root mean squared error was compared between the state of lithiation (SoL) predicted by the ML model and ground truth results from pore-scale direct numerical simulation (DNS) on unseen electrode configurations. It was shown that the ML model can predict the SoL at better than 99% accuracy in terms of relative error, but almost an order of magnitude faster than the DNS approach. The present work was limited to 2D cases but demonstrates that ML is a viable path forward for studying real 3D microstructures.

1. Introduction

Lithium-ion batteries are found in electronics ranging from cell phones, laptops, to electric vehicles (EVs) owing to their high energy density; though cost, limited range, and ability to fast-charge remain challenges, especially for mass EV adaptation [1]. One method of improving range would be to use higher capacity active materials, but this would involve research and development of novel chemistries and structures. Using currently available chemistries, one could naïvely add more active particles, but this would increase the capacity of a given only for a limited range of discharge rates [2]–[4]. It has been shown, however, that designing the cell architectures, by choosing a suitable particle-size distribution [3,5], specific particle placement [5], perforating electrodes [6], or combinations thereof, has the capability of improving cell performance by reducing losses due to concentration polarization. Designing these novel structures using computational tools would be preferrable, but the high computational cost is prohibitive so improved modeling techniques are of great interest.

A lithium-ion cell consists of a positive and negative electrode, which are both porous layers comprised of active particles (graphite on the negative electrode and a Li-alloy on the positive side) held together with a carbonaceous binder that provides electrical conductivity throughout the domain. The electrolyte fills the void space through which active species diffuse and migrate during operation. Understanding the structure-performance relationship in these porous electrodes is the key to developing or designing improved batteries. Numerical modeling is

* Corresponding author.
E-mail address: jgostick@uwaterloo.ca (J. Gostick).

https://doi.org/10.1016/j.apenergy.2024.122803
Received 12 August 2023; Received in revised form 8 January 2024; Accepted 1 February 2024

often employed in this regard, and by far the most widespread approach is the pseudo-two-dimensional (P2D) model, which incorporates concentrated solution and porous electrode theory [7,8]. Concentrated solution theory refers to the usage of molar flux equations from multi-component diffusion in liquids as described by the Onsager-Stefan-Maxwell equations. Porous electrode theory utilizes volume averaged properties of the electrode such as porosity, tortuosity, and effective electrical conductivity to model the transport in the through-plane direction. A pseudo second dimension arises since the model also considers the transport of Li ion in the solid phase by assuming spherical particles of active material. Due to the numerical simplicity and flexibility of the P2D model, many phenomena, such as thermal transport or mechanical deformation, have been coupled on top of the standard P2D model [9,10]. There are limitations when considering the porous electrode region as a homogeneous space. For example, a correlation must be used to account for the reduction in transport due to tortuosity through the porous structure. These correlations can be hard to measure, so substitutes are commonly used such as Bruggeman's relation despite known errors [11]. In place of correlations, it is possible to use experimentally measured transport processes, but these are not transferable between different microstructures.

As an alternative to P2D-type models, the direct numerical simulation (DNS) has been demonstrated with success [3,5,12]–[15]. DNS refers to conducting simulations on the exact internal geometry of the porous materials thus eliminating the need of effective quantities in contrast to porous electrode theory. For instance, a multiscale model utilizing the resolved microstructure with Li_xFePO_4 electrode nanoparticles from nano-X-ray computed tomography (XCT) revealed lithium intercalation occurring 10× faster in small constrictions than what the P2D model would have predicted [12]. More recently Lu et al. resolved both carbon binder and NMC111 active material domains using a dual-scan superimposition nano-XCT technique [5]. Their work investigated the value of using a graded structure near the separator along with a simulated enlarged pore structure. The results indicated high specific capacity even at high discharge rates, which is beneficial in applications which require high areal capacities such as EVs [16]. While pore-scale modeling elucidates the effects of heterogeneous microstructures, only a limited volume of the electrode can be resolved owing to memory limitations and prohibitive computational runtimes. For instance, Lu et al. considered a ($43 \times 43 \times 50\ \mu m$) representative volume element [5], and Xu et al. a ($30 \times 30 \times 40\ \mu m$) volume [13]. Run times are reported in the 10 to 30 days range, depending on the computer resources available.

There is a strong need to obtain higher-fidelity predictions compared to the P2D model yet to do so in more reasonable computational runtime than currently used microstructure-resolved DNS. Efforts have been made in this direction though the use pore network modeling (PNM) which was able to obtain good agreement with experimental discharge data, with simulation times in the range of hours instead of days or more compared to a DNS approach [17]. However, the PNM approach still requires a network extraction step, which is time-consuming especially for large domains. Also, while PNM is quicker than DNS it is still time-consuming for transient multiphysics simulations such as simulating battery discharge since it involves many iterations to deal with non-linearities/coupling and many time steps.

An alternative approach to be explored in this work is to use a machine learning method (ML) to predict key outputs, such as state-of-lithiation (SoL). ML and, more specifically, deep learning (DL) have recently gained traction due to the advances in modern computing power and thus have been used in various fields, achieving state-of-the-art results in various domains; in particular, the convolutional neural network (CNN) architecture has been successful in image-based learning tasks such as detection, segmentation, and object recognition [18]. Several works utilized ML methods to predict the velocity fields in porous media [19]–[21]. It should be mentioned that Wang et al. [19] and Santos et al. [20] cautioned against directly using the velocity field predictions from their neural networks (NN), but both had promising results in terms of predicting permeability from images, and Santos et al. suggested the resultant velocity field is best used as an initial guess in a lattice Boltzmann solver to accelerate convergence, and they demonstrated a 10× speed-up.

In parallel to the work on simulating transport as outlined above, there has been rapid progress in the application of ML to Li-ion batteries. Predicting the state-of-charge based on minimal external data has received a lot of attention due to its obvious value to end users [22–24]. Additionally, the prediction of life-cycle and durability has become possible [25,26]. Recent work has focused on predicting performance using physics-based simulations. Such simulations can be useful for designing cells but can be computationally costly, so machine learning provides an avenue to accelerate this process. For instance, Tu et al. [27] trained a ML model using continuum-based performance simulations and were able to predict discharge curves as a function of C-rate. Yang et al. [28] advanced this approach substantially by training their model on direct numerical simulations of microstructural images, demonstrating the ability to predict the discharge curve as a function of the microstructural parameters such as particle size distribution. Although they used microstructural simulations to predict the macroscopic behaviour of the cell, they did not attempt to predict microstructural information such as the distribution of lithium (i.e., the state of lithiation) within individual particles. In a recent review, Li et al. [29] have highlighted the important role that ML prediction will play in predicting battery state-of-health and degradation. Performance degradation depends on many factors, including stresses within individual particles due to uneven lithiation gradients. To date ML technique have not been used to accelerate microstructural simulations. In this work, we explore the possibility of using an ML framework based on CNNs to predict the SoL of NMC111 in a half-cell configuration trained with data generated from pore-scale finite element simulations. Since this work is a preliminary investigation, we used a 2D domain and the NMC particles were assumed to be circular with a narrow size distribution. As will be shown below, the proposed framework successfully predicts the SoL in particles, utilizing relatively simple input and metadata which circumvents the need for time-consuming preprocessing. It was shown that the ML model can predict the SoL at better than 99% accuracy in terms of relative error, but almost an order of magnitude faster than the DNS approach. The lessons learned here can be used to motivate and direct the development of a more rigorous model including 3D images and realistic particles.

2. Background

2.1. Electrochemical model

In this work, a two-dimensional domain was considered as visualized in Fig. 1 (only the top half is shown), showing from left-to-right regions corresponding to lithium foil, porous separator, and particle-resolved positive electrode with circular NMC particles. During discharge, the foil acts as the anode and the NMC as the cathode. The governing equations for a homogeneous domain are described by the works of *Newman* et al. [2,7,8]. Though as the particles are resolved, instead of a reaction source term in the diffusion equation, the source/sink term resulting from lithium intercalation is instead described using a non-homogenous Neumann boundary through the Butler-Volmer equation as described by Xu et al. [13]. The model used here closely follows that of Xu et al. [13] so the detailed exposition of the governing equations is relegated to the Appendix.

Each electrode in the dataset consists of half-cells where the NMC particles are represented by polydisperse circles with varying radii randomly generated by a Random Sequential Addition (RSA) algorithm as described by Torquato [30] (using PoreSpy [31]). Circles were used as a first approximation since NMC particles have been reported as relatively spherical within literature [5,11,17]. 2-dimensional analysis of

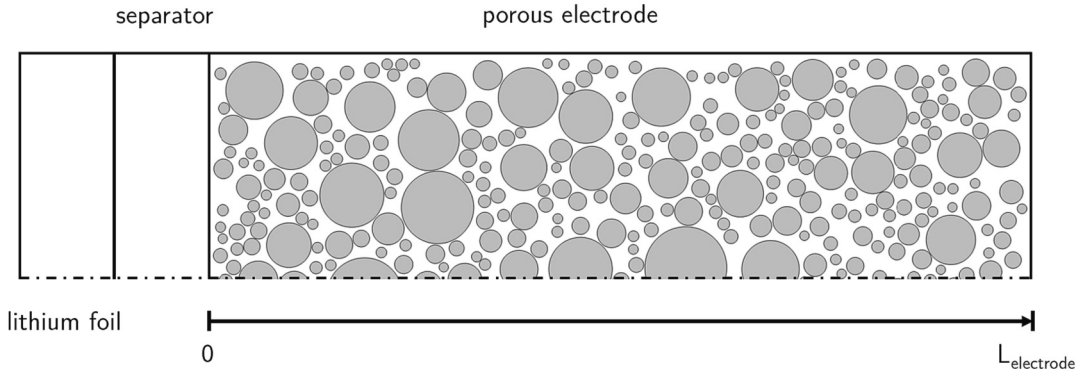

Fig. 1. Lithium-ion half-cell generated from the procedure as outlined in Appendix A. The regions represented in this figure are, from left to right: lithium foil, porous separator, and combined electrolyte-binder-NMC111 positive electrode. Only the top half of the electrode is shown in this figure.

other chemistries may require different geometries to be considered and a full 3-dimensional implementation could use voxel images obtained by X-ray tomography, but this is outside the scope of this preliminary study.

The discharge simulation of the domain shown in Fig. 1 was done by solving the system of equations mentioned in Appendix A. Fig. 2 illustrates several results that are of engineering interest: (a) the concentration of lithium ions in the electrolyte phase and (b) the lithium-ion concentration within the NMC particles under 3C-rate discharge. The magnitude of the lithium-ion concentration in the electrolyte and the resulting gradient is an indication of concentration polarization in the cell, and the concentration in the particles constitute the SoL. Although several variables were solved for by the DNS solver, only the solid concentration C_s as a function of time was tracked for training the model. This corresponds to figures similar to Fig. 2 (bottom), which for convenience we refer to as "SoL maps" (state-of-lithiation maps). The simulations were conducted at varied C-rates and were time-dependent studies, as such the CNN was tasked to predict the fractional SoL map in each particle given the C-rate and time step as well as additional inputs. As an aside, the definition of C-rate is the current density which discharges the cell at inverse of C hours (e.g., at a C-rate of 2, the cell discharges in half an hour). The concentration and time were exported from COMSOL for the purpose of creating a dataset amenable to training a CNN, and this will be discussed in the following section.

2.2. Dataset generation

Recall that the DNS solver stores SoL values at the FEM mesh nodes, so it cannot be directly fed into the CNN workflow. Therefore, the DNS results need to be processed into a pixel format, i.e., as a 2D array of SoL values. Additionally, instead of having the ML model to directly output the SoL map of an entire microstructure, the model predicts the SoL of isolated particles to facilitate the learning process, as illustrated in Fig. 3.

In this figure, the first column represents the SoL distribution within a cropped region obtained from the FEM solution, and the last column represents the processed SoL to be used for training the NN model. For this purpose, the FEM domain is first pixelized, i.e., turned into a 2D array of 0 s and 1 s, representing the electrolyte and NMC particles, respectively. It should be noted that the NN model developed in this work was designed to predict the SoL of the center particle in each cropped out region. In Fig. 3 (right), however, the SoL values for the neighboring particles are also shown, but only for illustration purposes. The following sections elaborate on the data processing steps.

2.2.1. Electrodes used in training

Starting from the DNS solution, the concentration of lithium in each NMC particle was saved from the simulations and normalized by the maximum intercalated lithium concentration, $C_{s,max}$, to obtain the fractional SoL. The ML dataset comprised of data from 60 random microstructure realizations in form of circle packings with lengths of 48, 77, 101, 129, 154, and 176 μm, a constant width of 100 μm, porosities between 35% to 60%, and particle radii between 1 and 10 μm. FEM simulations of galvanostatic discharge were performed on these microstructures at 5C-rates of 0.25, 0.5, 1, 2, and 3C. SoL values were evenly sampled 12 times during discharge based on the theoretical time to fully discharge a cell at the specified C-rate. For demonstration, the specifications of 5 out of 60 microstructures are tabulated in Table 1.

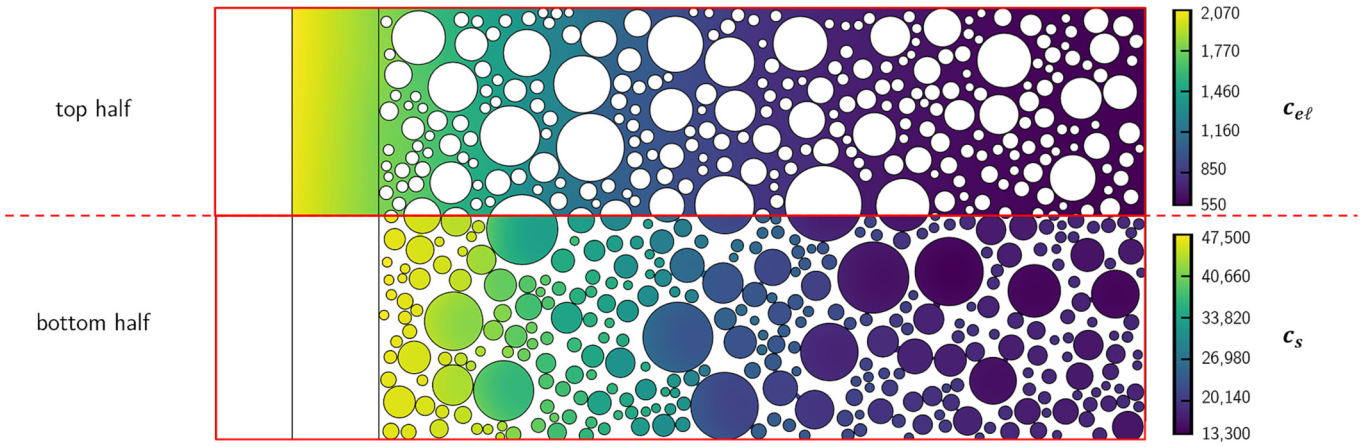

Fig. 2. Results from FEM simulation for the microstructure in Fig. 1 under 3C-rate discharge at t = 600 s. $C_{e\ell}$ and C_s are the lithium-ion concentration in the electrolyte and NMC phase, respectively.

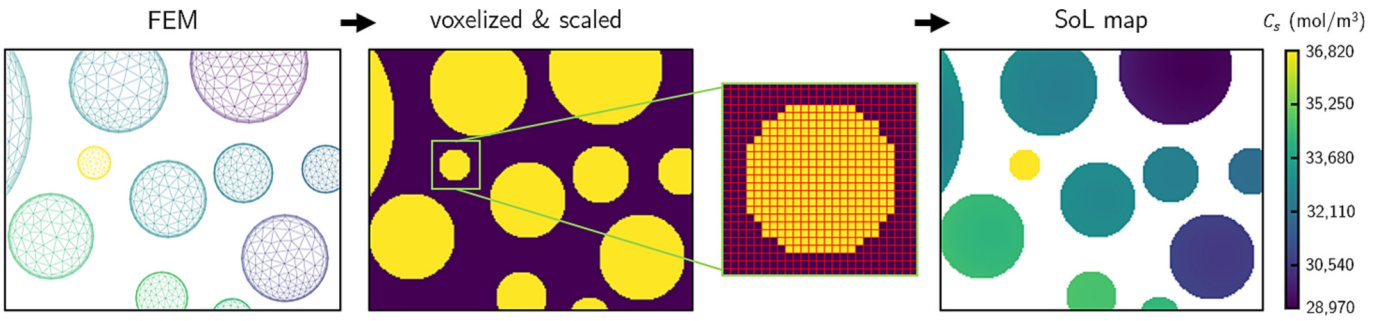

Fig. 3. Data processing steps from the DNS solution (left) to a binarized image of the electrode microstructure (middle) to the target SoL map (right). The NN model only considers the SoL of the center particle for training/prediction, and the SoL of the neighboring particles is only shown here for illustration purposes.

Table 1
Specification of five microstructures seen during training.

	Microstructures				
	I	II	III	IV	V
Length (μm)	154	176	48	176	129
Number of Particles	247	531	118	287	317
Porosity	0.55	0.43	0.49	0.53	0.58
Tortuosity	1.64	1.80	1.79	1.63	1.50
Mean Radius (μm)	2.53	1.97	2.12	2.50	2.91

2.2.2. Generating dataset: voxelization of microstructural images and SoL maps

The developed NN model takes in a binary image that represents the electrode microstructure with 0 s and 1 s representing the electrolyte and the NMC particles, respectively, and outputs an image of the same size with each representing the corresponding SoL. For each FEM simulation, the center coordinates, and the radii of the NMC particles are known. For creating the input images, using this information, disks were inserted into an empty image (initially filled with 0 s) with each disk representing an individual NMC particle. We scaled the coordinates to obtain a resolution of 0.2 μm per pixel. For the outputs, since the FEM simulations were conducted on an unstructured triangular mesh, we used SciPy's interpolate module to interpolate these values on an orthogonal grid to create 2D images of SoL.

2.2.3. Generating dataset: isolation of particles

In addition to the binary image, the Euclidian distance transform (EDT) of the input image, as shown in Fig. 4 (left), was fed to the NN model since it has been shown to facilitate the training [32,33]. As mentioned in previous sections, the NN model was designed to predict SoL for individual particles. Note that, however, that the layout of the neighboring particles affects mass transport and consequently the SoL of the particle of interest. Therefore, the neighboring particles were also included in the input image to make NN predictions more robust. To standardize how many particles to include, starting from the center of an arbitrary particle of interest with a radius of R_i, the width and height of the input image was defined by $3R_i$. Since the particle sizes are distributed between 1 μm and 10 μm, the extracted images will have different sizes. To standardize the inputs, the resulting images were scaled to be 150 by 150 pixels using the nearest neighbor interpolation. The zoom factor for each image was recorded and fed to the NN model as metadata, which will be discussed in the following sections. Finally, since each input image consists of many particles, only one of which is of interest, watershed segmentation was used to generate a mask to identify the particle of interest [34], as shown in Fig. 4 (middle), which is later used by the NN model to only return the SoL for this particle, as shown in Fig. 4 (right).

2.2.4. Metadata

In addition to the image-based inputs to the CNN, a feature vector was fed into the network to predict the SoL. This vector consists of 4 parameters found necessary for the network to predict the dynamic nature of cell operation and the other 5 may be considered as metadata to facilitate the learning process. The parameters constituting the feature vector are tabulated in Table 2. The critical parameters were time, C-rate, zoom factor, and distance from separator. Many of the same images may be fed to the network which correspond to a particle of interest, but battery discharge is transient, thus without the time and C-rate parameters the output would be multimodal. Regarding distance from separator, during discharge the particles near the separator will reach a higher SoL sooner than the particles near the current collector so the distance from the separate was included in the metadata [3,13]. Additionally, smaller particles typically experience uniform lithiation whereas larger particles would have a larger concentration gradient, so the particle radius was provided [3,13]. It is a common practice to scale each variable to a standard range (i.e., 0→1) to help ML models better learn the data [35]. These features are all trivial to obtain to do not

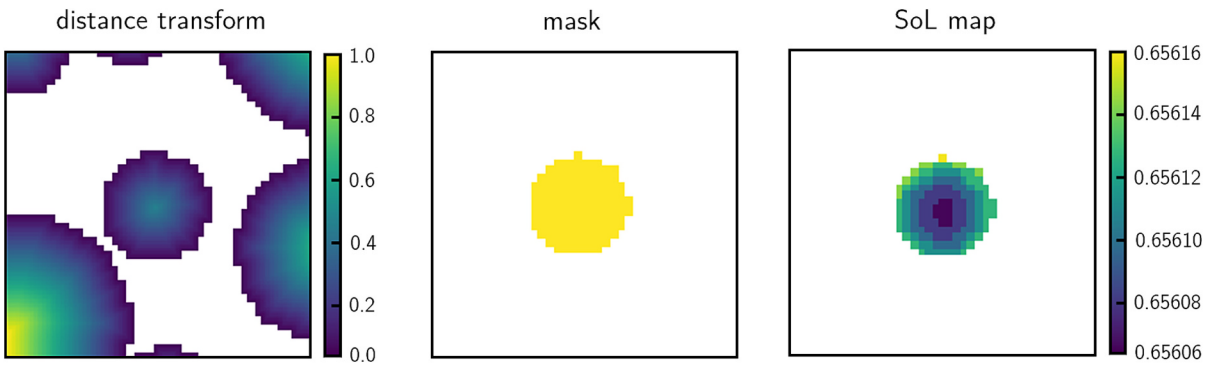

Fig. 4. Each input image (left) is a cut-out of a region of the microstructure centered around a particle followed by the Euclidian distance transform. The figure in the middle is the mask of the particle of interest and the one on the right is the SoL map for the respective particle.

Table 2
Features (metadata) used in the ML model to aid with predicting SoL.

Features	Normalization Value	Description
x	1	x-coordinate of center of particle (1)
y	100	y-coordinate of center of particle (μm)
R	10	radius of NMC particle (μm)
L	176	length of electrode (μm)
zoom factor	9	discussed in text
C-rate	3	discussed in text
time	14,400	time since discharge (s)
distance from separator	1	discussed in text
porosity	1	discussed in text

require any computational resources that would undermine the speed-up obtained by the model.

2.3. Machine learning model

The ML workflow in this work was written in Python and using the TensorFlow library. We used an autoencoder architecture to build the NN model. This architecture is composed of two parts, the encoder and the decoder as shown in Fig. 5. The encoder takes in a 2D image as input and compresses it by consecutively applying convolutional filters followed by max pooling, which eventually results in a 1D array of compressed information. The decoder part, which is essentially the encoder but in reverse order, takes in this 1D array and decompresses it to eventually reconstruct a 2D image of the same size as the input. An additional convolutional layer with the sigmoid activation function was added so the output would be bounded between 0 and 1. Finally, the feature vector was introduced to the NN model by adding to the compressed 1D array at the bottleneck section, i.e., the junction between the encoder and the decoder.

A common practice within ML is to split the overall dataset into training, validation, and test datasets. The model is optimized using the training set, and the validation set helps fine-tune its hyperparameters. In this work, the dataset was randomly shuffled, so all 60 microstructures were included in both the training and validation sets. However, a more sensible approach would have been to shuffle on an electrode basis, so that the training and validation sets were comprised of entirely different microstructures. To address this, a separate small dataset was created for testing. This ensured that the model's performance, illustrated in Fig. 6, could be evaluated on truly unseen microstructures. Further details will be provided in subsequent sections.

3. Results

3.1. Generation of ground truth data

FEM simulations were performed on a 2021 MacBook Pro with the Apple M1 Pro chip. Generation of 60 electrodes with 5C-rates until 100% Depth-of-Discharge (DoD) took ~26 h The proposed ML workflow was benchmarked against FEM and tabulated for a half-cell

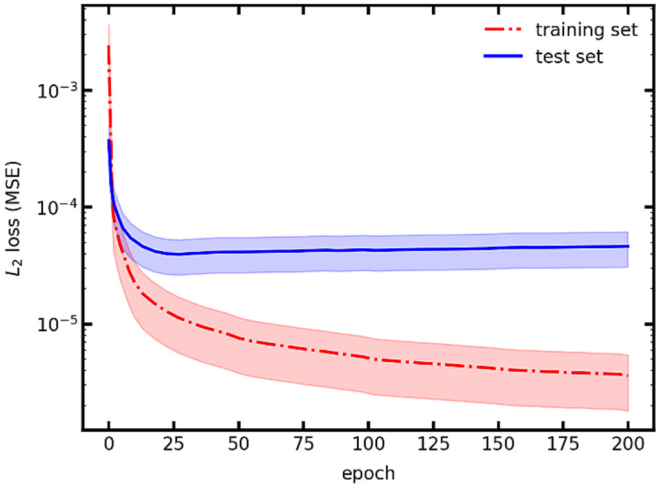

Fig. 6. Training data from the randomly shuffled dataset on a per image basis, 70% of the overall dataset was used (blue triangle markers). The red star markers represent data from two electrodes generated separately and is unseen data. The shaded regions are one standard deviation of loss values obtained from three independent trainings. The two-electrode dataset loss suggests that optimal model performance occurs at around epoch 25. (For interpretation of the references to colour in this figure legend, the reader is referred to the web version of this article.)

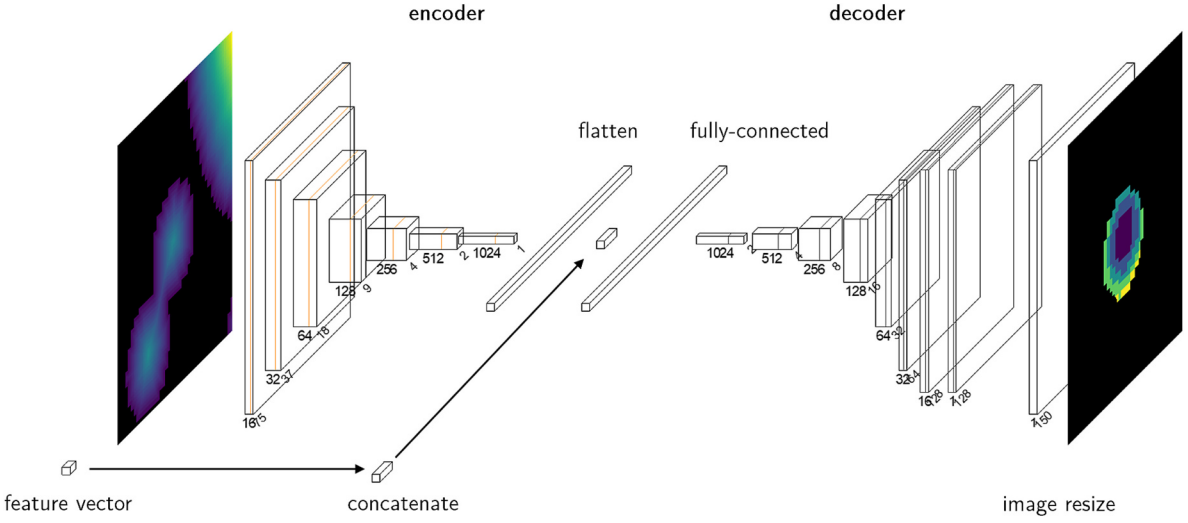

Fig. 5. The CNN-based autoencoder architecture used in this study. The images on the left and right are the input and target images, respectively. The orange and gray blocks represent Conv2D with max pooling and Conv2D with resizing layers each activated with ReLU. Purple, blue, and yellow are flatten, feed-forward with ReLU activation, and image resizing operations. (For interpretation of the references to colour in this figure legend, the reader is referred to the web version of this article.)

configuration as per Table 3. This benchmark suggest that the proposed workflow is on average an order of magnitude faster than the DNS solution. Based on Table 3, the ML runtime for the C-rate of 0.25 is almost twice that of other C-rates. This extra overhead is because the first run involves two additional steps for computing the distance transform and the watershed transform of the input image, which are then cached to speed up predictions at other C-rates. The results indicate that the FEM runtime decreases with increasing C-rate while the ML model has a relatively constant runtime around 65 s. Increasing the C-rate decreases the discharge time so the DNS solver would have to perform less time-stepping whereas the ML framework typically outputs 12 SoL maps. It should be noted that the metadata incorporated in this work is relatively simple (see Table 2), with the most time-consuming metric computed being the zoom factor. If a three-dimensional surrogate would be constructed with this ML approach, convolutions would run in linear time. In comparison, solving the assembled matrices in the DNS run in either quadratic or cubic time depending on if an iterative or direct algorithm is used, respectively. Therefore, an even more significant speed-up may be possible in implementing a three-dimensional model similar to the model presented here.

3.2. Model training

A total of 60 electrodes were generated, on which battery discharge was simulated using FEM at the following C-rates: 0.25C, 0.5C, 1C, 2C and 3C. The resulting dataset had 1,009,065 samples which were generated by taking snapshots of the solution for a particular electrode and C-rate at different time steps. 70% of the data were used for training, 15% for validation, and the remaining 15% for testing. The inputs and targets were represented as pixel images, and the values were scaled between $(0, 1)$. The model was trained by minimizing the loss function as per:

$$\mathscr{L} = \frac{1}{N_s N_x N_y} \sum_{k=1}^{N_s} \sum_{i=1}^{N_x} \sum_{j=1}^{N_y} \left(\widehat{Y}_{kij} - Y_{kij}\right)^2 \tag{1}$$

where N_s is the number of samples, and N_x and N_y are the number of pixels along x and y axes, respectively. In simple terms, the loss function, $\mathscr{L}$, is defined as the mean squared error (MSE) between the predicted SoL and the ground truth SoL values from FEM simulations. N_{pixels} are the number of pixels in the output image. The NN was trained using a stochastic gradient descent approach. We used the Adam optimizer [36] with a batch size of 256 (to saturate the GPU memory for optimal performance) with an initial learning rate of $LR = 10^{-6}$, $\beta_1 = 0.9$, $\beta_2 = 0.999$, and $\varepsilon = 10^{-7}$. The network was trained for 200 epochs where the learning rate was scheduled to halve every 50 epochs with an exponential decay between each epoch [37]. The training and validation loss were computed across the respective datasets after each epoch.

In terms of optimized hyper-parameters, two candidate autoencoder models were compared, the first with 16, 32, 64, 128, 256, and 512 filters and the second with an additional layer with 1024 filters, depicted in Fig. 5. The latter was chosen as it had a lower training and validation loss of 2.52×10^{-6} and 3.89×10^{-5} compared to 8.63×10^{-6} and 2.95×10^{-5}. The NN was trained using TensorFlow v2.10 on a server computer with a 2.10 GHz Intel Xeon CPU and two Nvidia Quadro RTX 8000 48GB GPUs. Each epoch on average took 428 s for a total training time of 1428 min.

Table 3
Run time comparison between the ground-truth FEM and the ML-based framework, conducted on an electrode with a length of 176 μm, porosity of 0.435, tortuosity of 1.86, and a total of 553 particles.

C-Rate	FEM runtime (s)	ML runtime (s)	Speedup
0.25	954	104.24	9.2
0.5	838	66.54	12.6
1	730	65.50	11.1
2	539	64.69	8.3
3	427	65.30	6.5

3.2.1. Loss curves

Fig. 6 shows the loss curves for training and test datasets. It should be noted that this curve is not from the model training but was constructed post hoc. The training data in the figure was obtained in a similar fashion to the training data used during model training, viz. a 70% random shuffling on a per sample basis. The test data shown represents data generated from two electrodes separately from the original 60 electrode with new random particle arrangements.

Based on this figure, the training loss is decreasing indefinitely while the test loss is at its minimum at around epoch 25, and then starts to increase. This indicates that the model starts to overfit (i.e., memorize the features in the training dataset) at epoch 25 and therefore, the model state at this stage was stored for later evaluations and is referred to as the "best model".

3.3. Model evaluation on single particles

To evaluate the best model in physical terms rather than just reporting the L_2 loss, we computed the average relative error of SoL for both the training and test datasets. The average relative error, also known as the mean absolute percentage error (MAPE), is defined in Eq. (2).

$$\text{MAPE} = \frac{1}{n} \sum_{k=1}^{N_s} \sum_{i=1}^{N_x} \sum_{j=1}^{N_y} \frac{\widehat{Y}_{kij} - Y_{kij}}{\widehat{Y}_{kij}} \tag{2}$$

For the training set, the average relative error was evaluated to be $\sim 0.3\%$, which is not surprising since the NN model has already "seen" them during training. For the test set, which have not been seen by the NN during training, the average relative error was still less than 1%. This performance indicates that the NN model has been able to generalize well beyond the training set. For qualitative demonstration, Fig. 7 shows the SoL values for isolated particles predicted by the NN model against ground truth for randomly selected particles at different time points and C-rates, accompanied by the respective relative error computed at individual pixels. Based on our analyses and as confirmed by this figure, not only the average relative error for the entire test dataset is below 1%, but that for individual particles and even individual pixels within each particle is still maintained below 1%.

Since concentration gradients within the particles have been shown to correlate to stress [14] and therefore degradation, it is of interest to see if the ML model is able to predict such gradients. Although the results presented in Fig. 7 show an acceptable agreement between ML predictions and ground truth for SoL, it is difficult to judge model accuracy for SoL gradients, especially that such gradients are very subtle within each particle and therefore, the colour bar needs to be rescaled to minimum and maximum SoL of individual particles. One challenge when analyzing gradients in the present work is due to the pixelated nature of the particle images, leading noisy derivatives. Matching gradients was not included in the training in the present work, though recent work has explored this possibility in general terms [38,39]. Since SoL gradients within particles are relevant to Li-ion performance, this approach offers great potential for future improvements on the current approach.

3.4. Comparison on whole electrode

Thus far, an ML model has been trained to predict the SoL for isolated particles in a given electrode microstructure using the procedure described in **Section 2.2** and with representative results shown in Fig. 7. However, the current form is not of practical use, so the predicted images must be recombined to create a continuous SoL map for the entire

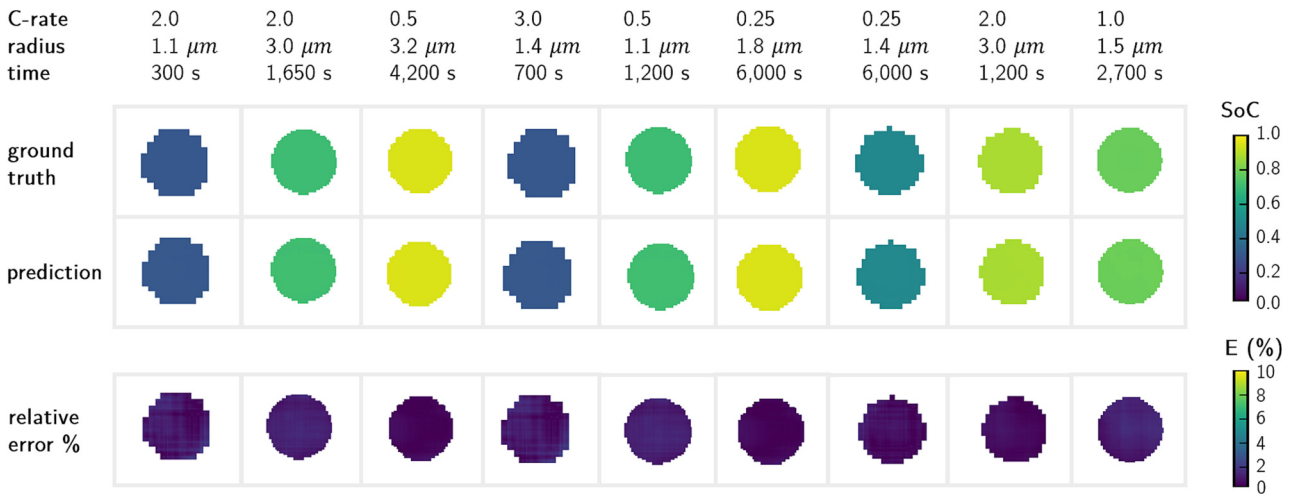

Fig. 7. Comparison of ML predictions for SoL against ground truth for randomly selected particles from the test dataset.

electrode. Fig. 8 shows the SoL map for the entire electrode at different C-rates at 50% depth of discharge as predicted by the ML model and compared against the FEM solution for a microstructure randomly selected from the test dataset. The ML predictions in this figure have been reconstructed, i.e., the ML model was used to predict the SoL map for individual particles and in the end, they were combined to generate the SoL map shown in this figure. Based on this figure, the average relative error is consistently below 5%, which indicates that the ML model has been able to generalize beyond the training dataset with an acceptable accuracy. Although the average relative error for all three C-rates is below 5%, the results show higher error as C-rate increases. To explain this behaviour, note that NN models tend to perform better when data is continuous and smooth [40,41]. Consequently, relatively sharp gradients are more difficult to capture for NN models. In the context of this work, discharging a battery at high C-rates leads to a Li concentration distribution with relatively sharp gradients near the separator, which possibly explains the worse performance of the ML model at high C-rates.

Turning attention now to the spatial distribution of SoL on the electrode scale, Fig. 9 shows the plane-averaged SoL as a function of distance from the separator at 3C (left), 1.5C (middle), and 3.5C (right) discharge rates and at the theoretical 50% depth of discharge, i.e., $t = 900\,s$, for an unseen microstructure. The shaded red region represents one standard deviation of SoL values for the FEM solution at the x-axis along the through-plane direction while the solid line and markers represent the average SoL at that point for FEM and ML model, respectively. Note that 3C discharge rate was already seen during training unlike 1.5C and 3.5C, which were chosen to evaluate the generalizability of the ML model in the interpolation and extrapolation regimes, respectively.

Based on this figure, the maximum relative error for 3C, 1.5C, and 3.5C discharge rates were calculated to be 5%, 4.5%, and 15%, respectively, which suggests good agreement in the interpolation regime, and acceptable agreement in the extrapolation regime. This

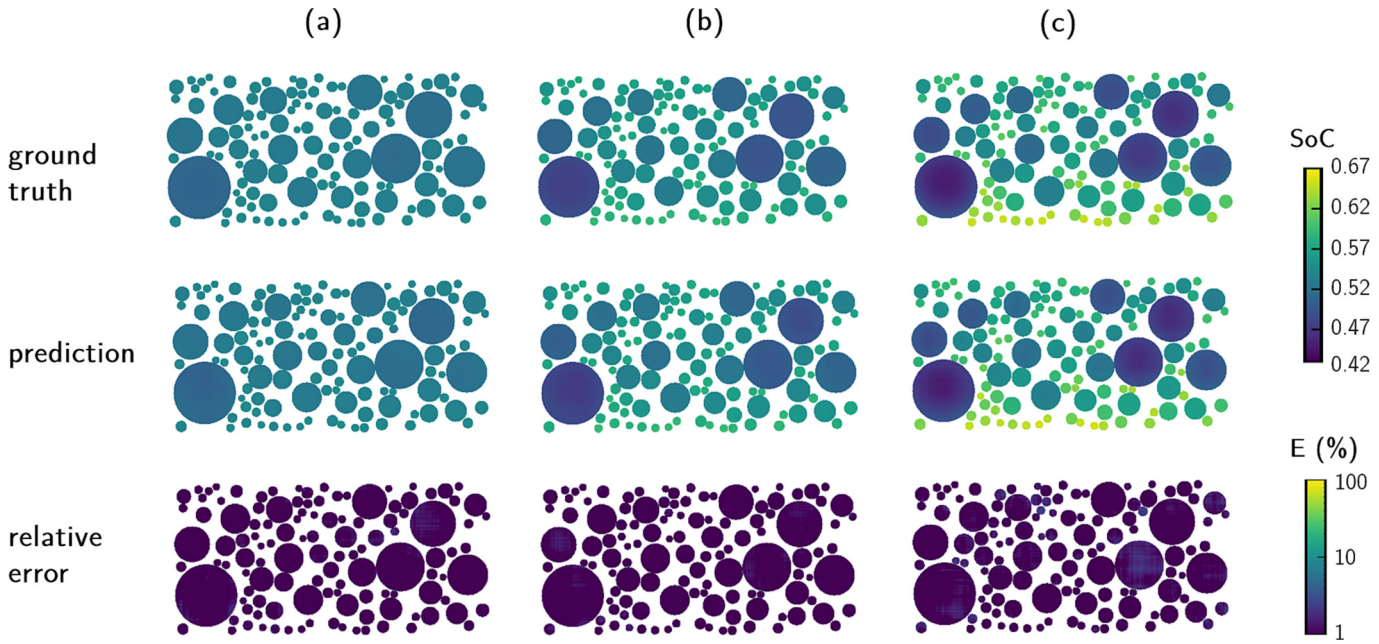

Fig. 8. SoL (colorbar) at 50% discharge capacity based on C-rates, current flows from left to right. The generated solmaps are for microstructure 3, as tabulated in Table 1. Column (a) is for 0.25C at 7200 s, (b) is for 1C at 1800s, and (c) is for 3C at 600 s. The top row shows the FEM simulation, the middle row shows the CNN prediction and the bottom row shows the relative % error.

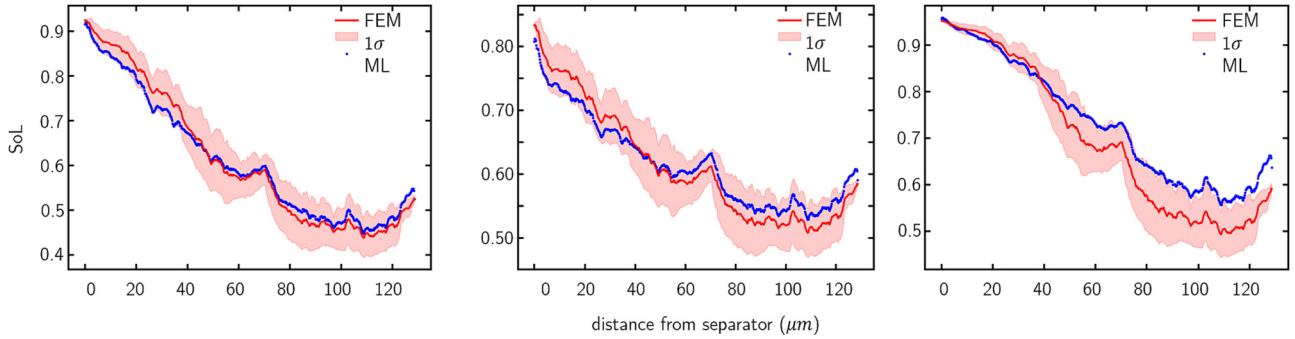

Fig. 9. Plane-averaged SoL distribution for an unseen microstructure at 3C (left), 1.5C (middle), and 3.5C (right) discharge rates at 50% depth of discharge (t = 900s) as a function of distance from the separator. The solid line is the FEM solution, and the blue dots are ML predictions. The shaded region shows one standard deviation of SoL values for the FEM solution. (For interpretation of the references to colour in this figure legend, the reader is referred to the web version of this article.)

sharp increase in relative error in the extrapolation regime is not surprising since NN models typically perform best when operating in the interpolation regime [42,43]. To help the NN model to extrapolate, one could use physics informed neural networks (PINNs), which at its core involves adding a physics-based term to the loss function [44,45], but that is beyond the scope of this work.

4. Conclusions

A machine learning framework was developed to explore the possibility of predicting the state-of-lithiation within the NMC particles of a Li-ion battery electrode. The model was intended as a surrogate with the aim of rapidly predicting the SoL given a new microstructure to avoid the use of computationally expensive direct numerical simulations. To simplify this task in this proof-of-concept study, the particles were assumed to be circular, with radii between 1 and 10 μm, and with a porosity range of 35–60%. For establishing ground truth values required for training the ML model, FEM simulations of battery discharge were conducted at various C-rates and depth of discharge. As for the ML model, an auto encoder convolutional neural network was used and trained on the data generated from FEM simulations. The inputs to the ML model were the binary image representing the microstructure, as well as its Euclidean distance transform, which was used to facilitate the training. To further aid the training, additional metadata was also extracted and fed to the ML model, such as distance from the separator. The ML model was designed to predict the SoL for isolated particles rather than for the entire electrode microstructure. For this reason, to predict the SoL for the entire electrode, the model needs to be run multiple times and the results pieced back together to reconstruct the entire electrode. Due to this approach, we evaluated the model performance at two levels: isolated particles, and the entire electrode. For the former, the model was shown to be able to predict the SoL of individual particles with a reasonable accuracy, although it was less successful at predict the concentration gradient in larger particles at high C-rates. For the latter, however, the model was able to accurately capture the SoL distribution across the entire electrode with a good accuracy. We also evaluated the performance of the ML model in predicting the SoL for C-rates unseen during the training. We tested different C-rates both in the interpolation and extrapolation regimes. In the former, the model performed very similar to those C-rates seen during training with a maximum relative error of 5% (for a particular unseen microstructure), while in the latter, the model accuracy dropped although it still maintained within an acceptable range with a maximum relative error of 15% (for the same microstructure). Conventional methods of predicting state-of-lithiation within electrode particles solve partial differential algebraic equations using numerical methods such as the finite element method. The main benefit of this framework was to reduce the computation time to predict the state-of-lithiation for battery discharge in heterogeneous models. Our benchmarks indicate that computation time is at least an order of magnitude quicker in comparison to finite element simulations, and we expect even higher speedups in the 3D case. One limitation of the current work, aside from being limited to 2D and spherical particles, is that the relatively small error achieved in concentration (SoL) predictions could still potentially lead to large errors in the concentration *gradient*. Recent work on incorporating gradients or spatial derivatives in the training process [38,39] is particularly relevant to the application of NNs to Li-ion electrodes since the lithiation gradient is particularly relevant for predicting stress-induced particle cracking. This work is a proof-of-concept which indicates that machine learning models could be a viable alternative to study battery behaviour, although we considered a simplified circular geometry for NMC particles as a first approximation. Future work in this area could investigate the use of machine learning to study battery discharge behaviour on real tomography images.

CRediT authorship contribution statement

Sam Ly: Writing – original draft, Visualization, Validation, Software, Methodology, Investigation, Formal analysis, Data curation. **Mohammad Amin Sadeghi:** Writing – review & editing, Writing – original draft, Validation, Software, Methodology, Investigation, Formal analysis, Data curation. **Niloofar Misaghian:** Software, Resources, Data curation. **Hamed Fathiannasab:** Validation, Software, Methodology, Formal analysis, Data curation. **Jeff Gostick:** Writing – review & editing, Writing – original draft, Validation, Supervision, Software, Resources, Project administration, Investigation, Funding acquisition, Conceptualization.

Declaration of competing interest

As the corresponding author I confirm that the authors have no competing interests to declare.

Data availability

Data will be made available on request.

Acknowledgement

The authors would like to acknowledge the Natural Science and Engineering Research Council of Canada (NSERC) for providing financial support for this project via the Discovery Grant program CREATE ME2, and CGSM Scholarshi (SL), as well as the CANARIE Software Reuse progam via RS3-141.

Appendix A. FEM battery discharge simulations

A.1. System of governing equations

The model used in this work closely follows that of Xu et al. [13] who performed microstructural simulations on tomographic images of electrodes. The governing equations for simulating battery discharge involve coupling concentration and potential fields. Lithium ions in the electrolyte phase move due to diffusion and migration, the former occurs due to a concentration gradient and the latter to the presence of a potential field in the electrolyte phase. Lithium ions intercalate into the NMC particles, described by Fick's law. The boundary condition is a non-homogenous Neumann condition described by Butler-Volmer kinetics. In this configuration, the NMC electrode behaves as the positive electrode, thus there is a net flux of lithium ions into NMC particles during discharge. The following diagram sums up the governing equations and boundary conditions used here and described in the following subsections.

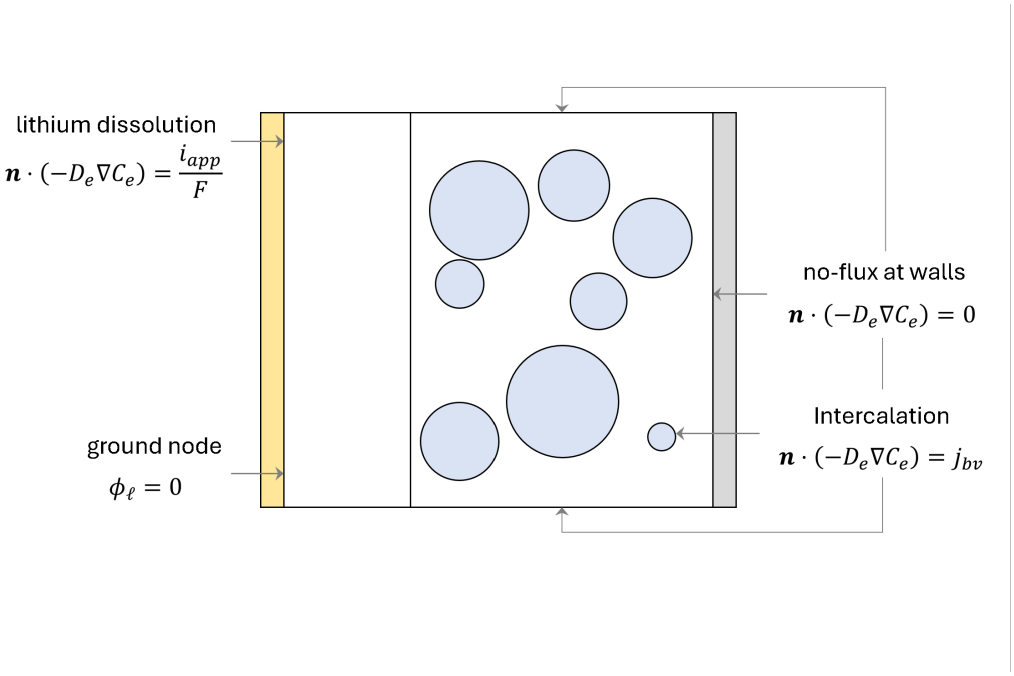

Fig. 10. Schematic diagram of domain with governing equations and boundary conditions indicated.

Because only 2D domains were considered here it was not possible to have percolation of both the solid and void phase simultaneously, so a fictitious binder phase is superimposed onto the electrolyte phase in the positive electrode region to provide electrical conductivity for the electrical current. This was accomplished by assigning a non-zero electrical conductivity to the liquid electrolyte phase, which is a tactic used by other microstructural models [3,5].

A.1.1. Electrode kinetics

The rate of intercalation of Li into the NMC active particles was described by the Butler-Volmer equation:

$$j = j_o \left(exp\left[\frac{\alpha_a F \eta}{RT}\right] - exp\left[\frac{-\alpha_c F \eta}{RT}\right] \right) \tag{3}$$

The value of j_o, the exchange current density, is defined as:

$$j_o = (k_c)^{\alpha_a} (k_a)^{\alpha_c} \left(C_{s,max} - C_{s,surf}\right)^{\alpha_c} \left(C_{s,surf}\right)^{\alpha_c} \left(\frac{C_e}{C_{e,ref}}\right)^{\alpha_a} \tag{4}$$

The exchange current density, j_o, could be viewed as a reference kinetic parameter. The exchange current density is a function of the concentration of lithium ions as well as kinetic parameters [2,7,8]. $C_{s,surf}$ and $C_{s,max}$represent the intercalated lithium ions on the surface of NMC and maximum concentration of lithium ions in the active material host structure, and C_e, and $C_{e,ref}$ the concentration of lithium ion in the electrolyte phase and reference concentration taken to be 1 $\frac{mol}{m^3}$ [13], respectively. The kinetic parameters are k_a and k_c are the reaction rate constant of the anodic and cathodic directions of the lithium intercalation reaction, and a_a, and a_c are the Tafel coefficients, which has been reported to be equal in the anodic and cathodic direction [43], $\alpha_a = \alpha_c = 0.5$.

$$\eta = \phi_s - \phi_l - U\left(\frac{C_{s,surf}}{C_{s,max}}\right) \tag{5}$$

Then, the activation overpotential, η, depends on the solid- and liquid electrolyte-phase potentials, ϕ_s and ϕ_l, as well as the electrode potential of the material, U. This is constant in the case of "typical" conversion-based electrodes but depends on the concentration of lithium ions on the surface in the case of intercalation materials. The potential is defined as the thermodynamically reversible potential, though in practice, this data is obtained under very low discharge (or C) rates; 0.02C as reported in [12].

A.1.2. Lithium-ion transport in the electrolyte phase

Lithium-ion transport in the electrolyte phase is modeled using the Onsager-Stefan-Maxwell equations as typically used in Newman's framework [44]. In the void space of the electrode the current density is given by:

$$i_l = -\kappa\nabla\phi_l + \frac{2RT}{F}\kappa\left(1+\frac{\partial lnf_{\pm}}{\partial lnC_l}\right)\left(1-t_o^+\right)\cdot\frac{1}{C_l}\nabla C_l \tag{6}$$

where κ is the ionic conductivity varying with lithium concentration, $f_{\pm}$ is the mean molar activity coefficient of the electrolyte, and t_o^+ is the lithium-ion transference number.

In the microstructure-resolved model there are no sources or sinks for ionic current within.

the bulk electrolyte phase, so the conservation equation for current in the electrolyte phase is:

$$\nabla\cdot i_l = 0 \tag{7}$$

The governing equation for ion transport in the electrolyte was described by the following governing equation:

$$\frac{\partial C_l}{\partial t} = \nabla\cdot(D_{Li}\nabla C_l) - \frac{t_o^+}{F}\nabla\cdot i_l \tag{8}$$

where D_{Li} is the lithium-ion diffusivity in the electrolyte. Note that porosity and tortuosity of the electrode are not required since this effect arise directly from the fact that the microstructure is accounted for by the computation mesh.

The microstructure of the porous separator was not resolved however, so the conservation law includes its porosity and tortuosity:

$$\varepsilon_{sep,l}\frac{\partial C_l}{\partial t} = \varepsilon_{sep,l}^{1.5}\left(\nabla\cdot(D_{Li}\nabla C_l) - \frac{t_o^+}{F}\nabla\cdot i_l\right) \tag{9}$$

where $\varepsilon_{sep,l}$ is the void fraction of the electrolyte phase in the separator region. The Bruggeman approximation was used to relate tortuosity to porosity, $t_{sep} = \varepsilon_{sep}^{-0.5}$, yielding the $\varepsilon_{sep}^{1.5}$ term.

Lastly, then anode is treated as lithium foil which is commonly done experimentally to eliminate the confounding effects of anode performance on the results. The voltage in the liquid phase at the foil was taken as the ground:

$$\phi_l\left(x = x_{foil}, t\right) = 0\ V \tag{10}$$

Initial conditions

The initial conditions were as follows:

$$\phi_l = 0\ V$$

$$C_l(x, t=0) = 1000\frac{mol}{m^3} \tag{11}$$

At $t = 0$, the potential is $\phi_l = 0\ V$ and typical concentrations of lithium used in batteries is $C_{Li^+} = 1M$.

Boundary conditions

There are boundary conditions for both concentration and potential fields. At the lithium foil, the flux of lithium-ions is the applied current density, which is typically described using C-rates. The definition of C-rate is the current density which discharges the cell at inverse of C hours. So 1C would discharge the cell in 1 h and 2C would discharge the cell in half an hour. Then, the boundary condition at each particle is related to the Butler-Volmer equation:

$$-\vec{n}\cdot\Gamma_{\phi_l}\left(x = x_{foil}, t\right) = i_{app}$$

$$-\vec{n}\cdot\Gamma_{\phi_l} = j_{bv}F, \forall i \in P_i \tag{12}$$

where $\vec{n}$ is the normal vector pointing out of a domain, Γ_{ϕ_l} is a shorthand for the ionic migration term, i_{app} represent the applied current density specified in multiples of C-rate, and P_i represents the i particles in the positive electrode region:

$$-\vec{n}\cdot\Gamma_{C_l}\left(x = x_{foil}, t\right) = \frac{i_{app}}{F}$$

$$-\vec{n}\cdot\Gamma_{C_l} = j_{bv}, \forall i \in P_i \tag{13}$$

Similarly, Γ_{C_l} is a shorthand for Fick's law in the electrolyte region.

A.1.3. Lithium-ion intercalation

The solid phase refers to the lithium foil, current collector and the NMC particles. Concentration and potential are modeled in the NMC particle phase. Intercalation is modeled through Fick's law and potential through Ohm's law. The electrical conductivity of the NMC particle phase was adjusted to include the effect of conductive binder, though this was not explicitly resolved.

Lithium-ion transport in particles

Diffusion of Li-ions in the solid (NMC) phase was described using Fick's second law:

$$\frac{\partial C_s}{\partial t} = \nabla\cdot(D_s\nabla C_s) \tag{14}$$

where C_s is the lithium-ion concentration in the NMC host structure and D_s is the lithium diffusivity in the active particles.

Solid potential

Conservation of charge in the solid phase was applied as follows:

$$\nabla\cdot\left(-\sigma_{NMC+Binder}\nabla\phi_{s,NMC+Binder}\right)=0 \tag{15}$$

where σ is the electrical conductivity of the solid material. Again, this includes the fact that electronically conductive binder was not resolved separately from NMC particles.

Electrical ground

The ground node is selected to be at the lithium foil as in the solution-phase potential.

$$\phi_{s,foil}\left(x=x_{foil},t\right)=0\ V \tag{16}$$

And the boundary conditions at the particle interfaces being related to the Butler-Volmer equation.

Initial conditions

The concentration in the solid phase was assumed to be constant throughout:

$$C_s(x,t=0)=C_{s,0} \tag{17}$$

where $C_{s,0}$ is the initial lithium concentration in the NMC host structure. In addition, the initial potential of the conductive binder is assumed to be at the same potential as the NMC particles:

$$\phi_{s,NMC,+Binder}(x,t=0)=U_{NMC}\left(\frac{C_{s,0}}{C_{s,max}}\right) \tag{18}$$

Boundary conditions

The source of lithium ions from the electrolyte phase into the NMC particles is as represented with a Neumann boundary condition and the second boundary indicates there is no flux of lithium out of the domain:

$$-\overrightarrow{n}\cdot\Gamma_{C_s}=-j_{bv},\forall i\in P_i$$

$$-\overrightarrow{n}\cdot\Gamma_{C_s}(x=x_{current\ collector},t)=0 \tag{19}$$

where *Pi* are the NMC particles in the positive electrode region. There is electronic current at the electrolyte/NMC particle interface and the boundary condition at the current collector is the applied current density:

$$-\overrightarrow{n}\cdot\Gamma_{\phi_s}=-j_{bv}F,\forall i\in P_i$$

$$-\overrightarrow{n}\cdot\Gamma_{\phi_s}(x=x_{current\ collector},t)=-i_{app} \tag{20}$$

A.2. Electrochemical and cell parameters

Fig. 1 represents the cell geometry generated from the following outlined procedure. Cells could either be optimized towards energy or power where the former favours thicker and highly packed cells while the latter favours thin cells. In EVs, the trend is thin cells with high particle packings. This translates into cells with relatively low porosities of 0.32 to 0.37, readers could refer to Table I in [16] for a comprehensive overview. The separator lengths used in the simulations is taken to be 20 μm [13]. The physical parameters used in this work is tabulated in Table 4.

Table 4
Physical parameters for electrochemical simulations used in this work.

Parameter	Value [Ref]	Unit	Parameter	Value [Ref]	Unit
σ_{NMC}	100 [45]	S/m	$C_{s,0}$	980	mol/m^3
σ_{binder}	1	S/m	$C_{l,ref}$	1 [13]	mol/m^3
κ	$f(C_l)$, [2]	S/m	$C_{l,0}$	1000 [13]	mol/m^3
t_o^+	0.363 [46]	–	$\varepsilon_{sep,l}$	0.4	–
$\partial lnf_{\pm}/\partial lnC_e$	0 [2]	–	U	$f(C_s)$, [45]	V
k_c	2×10^{-11} [43]	m/s	D_{Li}	7.5×10^{-10}	m^2/s
k_a	2×10^{-11} [43]	m/s	D_s	5×10^{-13} [45]	m^2/s
α_c	0.5 [43]	–	SOC_{max}	0.975 [45]	–
α_a	0.5 [43]	–	SOC_{min}	0 [45]	–
$C_{s,max}$	48900	mol/m^3			

References

[1] Cano ZP, et al. Batteries and fuel cells for emerging electric vehicle markets. Nat Energy Apr. 2018;3(4):279–89. https://doi.org/10.1038/s41560-018-0108-1.

[2] Doyle M, Newman J, Gozdz AS, Schmutz CN, Tarascon J. Comparison of modeling predictions with experimental data from plastic Lithium ion cells. J Electrochem Soc Jun. 1996;143(6):1890–903. https://doi.org/10.1149/1.1836921.

[3] Lu X, et al. Multi-length scale microstructural design of lithium-ion battery electrodes for improved discharge rate performance. Energy Environ Sci 2021;14 (11):5929–46. https://doi.org/10.1039/D1EE01388B.

[4] Xu H, et al. Guiding the design of heterogeneous electrode microstructures for Li-ion batteries: microscopic imaging, predictive modeling, and machine learning. Adv Energy Mater May 2021;11(19). https://doi.org/10.1002/aenm.202003908.

[5] Lu X, et al. 3D microstructure design of lithium-ion battery electrodes assisted by X-ray nano-computed tomography and modelling. Nat Commun Apr. 2020;11(1): 2079. https://doi.org/10.1038/s41467-020-15811-x.

[6] Chen K-H, et al. Efficient fast-charging of lithium-ion batteries enabled by laser-patterned three-dimensional graphite anode architectures. J Power Sources Sep. 2020;471:228475. https://doi.org/10.1016/j.jpowsour.2020.228475.

[7] Doyle M, Fuller TF, Newman J. Modeling of Galvanostatic charge and discharge of the Lithium/polymer/insertion cell. J Electrochem Soc Jun. 1993;140(6):1526–33. https://doi.org/10.1149/1.2221597.

[8] Doyle M, Newman J. The use of mathematical modeling in the design of lithium/polymer battery systems. Electrochim Acta Oct. 1995;40(13–14):2191–6. https://doi.org/10.1016/0013-4686(95)00162-8.

[9] Deshpande R, Verbrugge M, Cheng Y-T, Wang J, Liu P. Battery cycle life prediction with coupled chemical degradation and fatigue mechanics. J Electrochem Soc Jan. 2012;159(10):A1730–8. https://doi.org/10.1149/2.049210jes.

[10] Ai W, Kraft L, Sturm J, Jossen A, Wu B. Electrochemical thermal-mechanical modelling of stress inhomogeneity in lithium-ion pouch cells. J Electrochem Soc Oct. 2020;167(1):013512. https://doi.org/10.1149/2.0122001JES.

[11] Ebner M, Chung D, García RE, Wood V. Tortuosity anisotropy in lithium-ion battery electrodes. Adv Energy Mater Apr. 2014;4(5). https://doi.org/10.1002/aenm.201301278.

[12] Kashkooli AG, et al. Multiscale modeling of lithium-ion battery electrodes based on nano-scale X-ray computed tomography. J Power Sources Mar. 2016;307:496–509. https://doi.org/10.1016/j.jpowsour.2015.12.134.

[13] Xu R, et al. Heterogeneous damage in Li-ion batteries: experimental analysis and theoretical modeling. J Mech Phys Solids Aug. 2019;129:160–83. https://doi.org/10.1016/j.jmps.2019.05.003.

[14] Fathiannasab H, Zhu L, Chen Z. Chemo-mechanical modeling of stress evolution in all-solid-state lithium-ion batteries using synchrotron transmission X-ray microscopy tomography. J Power Sources Jan. 2021;483:229028. https://doi.org/10.1016/j.jpowsour.2020.229028.

[15] Fathiannasab H, Ghorbani Kashkooli A, Li T, Zhu L, Chen Z. Three-dimensional modeling of all-solid-state lithium-ion batteries using synchrotron transmission X-ray microscopy tomography. J Electrochem Soc Jun. 2020;167(10):100558. https://doi.org/10.1149/1945-7111/ab9380.

[16] Gallagher KG, et al. Optimizing areal capacities through understanding the limitations of Lithium-ion electrodes. J Electrochem Soc Nov. 2016;163(2): A138–49. https://doi.org/10.1149/2.0321602jes.

[17] Khan ZA, Agnaou M, Sadeghi MA, Elkamel A, Gostick JT. Pore network modelling of Galvanostatic discharge behaviour of lithium-ion battery cathodes. J Electrochem Soc Jul. 2021;168(7):070534. https://doi.org/10.1149/1945-7111/ac120c.

[18] LeCun Y, Bengio Y, Hinton G. Deep learning. Nature May 2015;521(7553):436–44. https://doi.org/10.1038/nature14539.

[19] Da Wang Y, Chung T, Armstrong RT, Mostaghimi P. ML-LBM: predicting and accelerating steady state flow simulation in porous media with convolutional neural networks. Transp Porous Media May 2021;138(1):49–75. https://doi.org/10.1007/s11242-021-01590-6.

[20] Santos JE, Xu D, Jo H, Landry CJ, Prodanović M, Pyrcz MJ. PoreFlow-net: a 3D convolutional neural network to predict fluid flow through porous media. Adv Water Resour Apr. 2020;138:103539. https://doi.org/10.1016/j.advwatres.2020.103539.

[21] Hennigh O. Lat-net: Compressing lattice Boltzmann flow simulations using deep neural networks. May 2017.

[22] Tang A, Huang Y, Liu S, Yu Q, Shen W, Xiong R. A novel lithium-ion battery state of charge estimation method based on the fusion of neural network and equivalent circuit models. Appl Energy Oct. 2023;348:121578. https://doi.org/10.1016/j.apenergy.2023.121578.

[23] Yang Y. A machine-learning prediction method of lithium-ion battery life based on charge process for different applications. Appl Energy Jun. 2021;292:116897. https://doi.org/10.1016/j.apenergy.2021.116897.

[24] Lu J, Xiong R, Tian J, Wang C, Sun F. Deep learning to estimate lithium-ion battery state of health without additional degradation experiments. Nat Commun May 2023;14(1):2760. https://doi.org/10.1038/s41467-023-38458-w.

[25] Wang S, Fan Y, Jin S, Takyi-Aninakwa P, Fernandez C. Improved anti-noise adaptive long short-term memory neural network modeling for the robust remaining useful life prediction of lithium-ion batteries. Reliab Eng Syst Saf Feb. 2023;230:108920. https://doi.org/10.1016/j.ress.2022.108920.

[26] Wang S, Wu F, Takyi-Aninakwa P, Fernandez C, Stroe D-I, Huang Q. Improved singular filtering-Gaussian process regression-long short-term memory model for whole-life-cycle remaining capacity estimation of lithium-ion batteries adaptive to fast aging and multi-current variations. Energy Dec. 2023;284:128677. https://doi.org/10.1016/j.energy.2023.128677.

[27] Tu H, Moura S, Wang Y, Fang H. Integrating physics-based modeling with machine learning for lithium-ion batteries. Appl Energy Jan. 2023;329:120289. https://doi.org/10.1016/j.apenergy.2022.120289.

[28] Yang W, et al. Time-dependent deep learning predictions of 3D electrode particle-resolved microstructure effect on voltage discharge curves. J Power Sources Sep. 2023;579:233087. https://doi.org/10.1016/j.jpowsour.2023.233087.

[29] Li AG, West AC, Preindl M. Towards unified machine learning characterization of lithium-ion battery degradation across multiple levels: a critical review. Appl Energy Jun. 2022;316:119030. https://doi.org/10.1016/j.apenergy.2022.119030.

[30] Torquato S. Random heterogeneous materialsvol. 16. New York, NY: Springer New York; 2002. https://doi.org/10.1007/978-1-4757-6355-3.

[31] Gostick J, et al. PoreSpy: a Python toolkit for quantitative analysis of porous media images. J Open Source Softw May 2019;4(37):1296. https://doi.org/10.21105/joss.01296.

[32] Santos JE, Xu D, Jo H, Landry CJ, Prodanović M, Pyrcz MJ. PoreFlow-net: a 3D convolutional neural network to predict fluid flow through porous media. Adv Water Resour Apr. 2020;138:103539. https://doi.org/10.1016/j.advwatres.2020.103539.

[33] Santos JE, et al. Computationally efficient multiscale neural networks applied to fluid flow in complex 3D porous media. Transp Porous Media Oct. 2021;140(1): 241–72. https://doi.org/10.1007/s11242-021-01617-y.

[34] van den Berg EH, Meesters AGCA, Kenter JAM, Schlager W. Automated separation of touching grains in digital images of thin sections. Comput Geosci Mar. 2002;28 (2):179–90. https://doi.org/10.1016/S0098-3004(01)00038-3.

[35] Obaid HS, Dheyab SA, Sabry SS. The impact of data pre-processing techniques and dimensionality reduction on the accuracy of machine learning. In: 2019 9th annual information technology, electromechanical engineering and microelectronics conference (IEMECON). IEEE; Mar. 2019. p. 279–83. https://doi.org/10.1109/IEMECONX.2019.8877011.

[36] Kingma DP, Ba J. Adam: A method for stochastic optimization. Dec. 2014.

[37] Wang Y, Xiao Z, Cao G. A convolutional neural network method based on Adam optimizer with power-exponential learning rate for bearing fault diagnosis. J Vibroeng Jun. 2022;24(4):666–78. https://doi.org/10.21595/jve.2022.22271.

[38] Yu J, Lu L, Meng X, Karniadakis GE. Gradient-enhanced physics-informed neural networks for forward and inverse PDE problems. Comput Methods Appl Mech Eng Apr. 2022;393:114823. https://doi.org/10.1016/j.cma.2022.114823.

[39] O'Leary-Roseberry T, Chen P, Villa U, Ghattas O. Derivative-informed neural operator: an efficient framework for high-dimensional parametric derivative learning. J Comput Phys Jan. 2024;496:112555. https://doi.org/10.1016/j.jcp.2023.112555.

[40] Grinsztajn L, Oyallon E, Varoquaux G. Why do tree-based models still outperform deep learning on typical tabular data?. 2023.

[41] Rahaman N, et al. On the spectral bias of neural networks. 2023.

[42] Barnard E, Wessels LFA. Extrapolation and interpolation in neural network classifiers. IEEE Control Syst Oct. 1992;12(5):50–3. https://doi.org/10.1109/37.158898.

[43] Xu K, Zhang M, Li J, Du SS, Kawarabayashi K, Jegelka S. How neural networks extrapolate: From feedforward to graph neural networks. Sep. 2020.

[44] Kamrava S, Sahimi M, Tahmasebi P. Simulating fluid flow in complex porous materials by integrating the governing equations with deep-layered machines. Npj Comput Mater Aug. 2021;7(1):127. https://doi.org/10.1038/s41524-021-00598-2.

[45] Zhou X-H, McClure JE, Chen C, Xiao H. Neural network–based pore flow field prediction in porous media using super resolution. Phys Rev Fluids Jul. 2022;7(7): 074302. https://doi.org/10.1103/PhysRevFluids.7.074302.